Available online at www.sciencedirect.com
ScienceDirect
Geochimica et Cosmochimica Acta 74 (2010) 5966–5983
Geochimica et Cosmochimica Acta
www.elsevier.com/locate/gca

Mineral associations and character of isotopically anomalous organic material in the Tagish Lake carbonaceous chondrite

Thomas J. Zega [a,*], Conel M. O'D. Alexander [b], Henner Busemann [c], Larry R. Nittler [b], Peter Hoppe [d], Rhonda M. Stroud [a], Andrea F. Young [e]

[a] Materials Science and Technology Division, Naval Research Laboratory, 4555 Overlook Ave. SW, Washington, DC 20375, USA
[b] Department of Terrestrial Magnetism, Carnegie Institution of Washington, 5241 Broad Branch Rd NW, Washington, DC 20015, USA
[c] School of Earth, Atmospheric and Environmental Sciences, The University of Manchester, Manchester M13 9PL, United Kingdom
[d] Max Planck Institute for Chemistry, P.O. Box 3060, 55020 Mainz, Germany
[e] Department of Physics, Columbia University, NY 10027, USA

Received 17 August 2009; accepted in revised form 12 July 2010; available online 21 July 2010

Abstract

We report a coordinated analytical study of matrix material in the Tagish Lake carbonaceous chondrite in which the same small ($\leqslant$20 μm) fragments were measured by secondary ion mass spectrometry (SIMS), transmission electron microscopy (TEM), energy-dispersive X-ray spectroscopy (EDS), electron energy-loss spectroscopy (EELS), and X-ray absorption near-edge spectroscopy (XANES). SIMS analysis reveals H and N isotopic anomalies (hotspots), ranging from hundreds to thousands of nanometers in size, which are present throughout the fragments. Although the differences in spatial resolution of the SIMS techniques we have used introduce some uncertainty into the exact location of the hotspots, in general, the H and N isotopic anomalies are spatially correlated with C enrichments, suggesting an organic carrier. TEM analysis, enabled by site-specific extraction using a focused-ion-beam scanning-electron microscope, shows that the hotspots contain an amorphous component, Fe–Ni sulfides, serpentine, and mixed-cation carbonates. TEM imaging reveals that the amorphous component occurs in solid and porous forms, EDS indicates that it contains abundant C, and EELS and XANES at the C K edge reveal that it is largely aromatic. This amorphous component is probably macromolecular C, likely the carrier of the isotopic anomalies, and similar to the material extracted from bulk samples as insoluble organic matter. However, given the large sizes of some of the hotspots, the disparity in spatial resolution among the various techniques employed in our study, and the phases with which they are associated, we cannot entirely rule out that some of the isotopic anomalies are carried by inorganic material, e.g., sheet silicates. The isotopic composition of the organic matter points to an initially primitive origin, quite possibly within cold interstellar clouds or the outer reaches of the solar protoplanetary disk. The association of organic material with secondary phases, e.g., serpentine and carbonates, suggests that the organic matter was susceptible to parent-body processing, and thus, isotopic dilution.
Published by Elsevier Ltd.

1. INTRODUCTION

Carbonaceous chondrites (CCs) are heterogeneous aggregates of some of the most primitive early solar system materials available for investigation. They can contain a diverse suite of components including: chondrules and calcium–aluminum-rich inclusions (CAIs) that experienced transient heating events within the solar nebula (Connolly et al., 2006; MacPherson, 2005); presolar grains that formed via gas-phase condensation in circumstellar environments (Zinner, 2005); and carbonates and sheet silicates that formed through low-temperature aqueous-alteration

* Corresponding author. Tel.: +1 202 404 2082.
E-mail address: tzega@nrl.navy.mil (T.J. Zega).

0016-7037/$ - see front matter Published by Elsevier Ltd.
doi:10.1016/j.gca.2010.07.018

reactions on meteorite parent bodies (Brearley, 2005). Study of these primitive rocks can therefore provide insight into a wide range of presolar and early solar system environments and processes.

The C in CCs occurs in both organic and inorganic forms. Carbonates, graphite, SiC, and nanodiamond constitute the bulk of the inorganic C, whereas the organic fraction can be subdivided into material that is soluble or insoluble in polar and non-polar solvents, including demineralizing acids. The soluble fraction contains a large variety of organic compounds, e.g., aliphatic and aromatic hydrocarbons, amines, amides, carboxylic and amino acids, *N*-heterocycles, polyols, sulfonic acids, etc. (Gilmour, 2005; Pizzarello et al., 2006). In comparison, the insoluble fraction contains a mixture of nanodiamonds (a few percent of the C) and an organic component consisting of a high-molecular weight macromolecular material (Gilmour, 2005). This insoluble organic component, often referred to as insoluble organic matter or IOM, constitutes 70–99% of the organic material in CCs (Pizzarello et al., 2006). Isotopic anomalies in the IOM, namely excesses in deuterium (D) and ^{15}N, are believed to reflect the partial preservation of presolar molecules originally formed in the interstellar clouds or at the edge of the solar protoplanetary disk (Robert and Epstein, 1982; Yang and Epstein, 1983; Alexander et al., 1998; Messenger, 2000; Busemann et al., 2006b; Alexander et al., 2007; Floss and Stadermann, 2009; Remusat et al., 2009). Variations in isotopic and elemental chemistry among the IOM of different CC classes were hypothesized to represent parent-body processing of a common primitive organic precursor (Alexander et al., 2007, 2010).

Though not the most petrologically primitive meteorite, the Tagish Lake CC is, arguably, the best preserved, having been collected from frozen ice shortly after falling to Earth on January 18, 2000 (Brown et al., 2000). The mineralogy, isotopic, and bulk chemical composition of the Tagish Lake CC classify it as a petrologic type 2 chondrite but between that of CM and CI chondrites, making it a unique meteorite in terrestrial collections. Measurements of pristine samples show that it contains up to 5.8 wt% C, approximately 2.6 wt% of which is organic (Grady et al., 2002). Acid-dissolution experiments indicate that over 99% of the organic matter occurs in IOM form (Pizzarello et al., 2006), and nuclear magnetic resonance (NMR) spectroscopy on IOM residues suggest that it has abundant aromatic character (Pizzarello et al., 2001; Cody and Alexander, 2005). The bulk D and ^{15}N enrichments of the Tagish Lake IOM ($\delta D = 596 \pm 4‰$, $\delta^{15}N = 73 \pm 1.5‰$; Alexander et al., 2007), while significant, are lower than those observed in the IOM of CR and some CM chondrites. The smaller ^{15}N and D anomalies, together with the high aromatic fraction (relative to the CR, CI, and CM chondrites), suggests that Tagish Lake IOM has been affected by parent-body processing. However, isotopic imaging by secondary ion mass spectrometry (SIMS) revealed that IOM in CCs is isotopically heterogeneous, with sub-μm- to μm-sized regions highly enriched in D and/or ^{15}N ('hotspots'), relative to the bulk IOM. In the Tagish Lake CC, hotspot values reach $\delta D = 15{,}000‰$ and $\delta^{15}N = 1000‰$ (Ashley et al., 2005; Nakamura-Messenger et al., 2006; Busemann et al., 2006b; Herd et al., 2009). These values are comparable to those observed in interplanetary dust particles (Messenger, 2000), suggesting very primitive origins (Busemann et al., 2006b). The carrier of the isotopic anomalies in Tagish Lake IOM has, in part, been linked to discrete, hundreds of nanometer- to micron-sized, often hollow spheres ('nanoglobules') which contain a strong aromatic component (Nakamura et al., 2002, 2004; Garvie and Buseck, 2004; Messenger et al., 2004; Ashley et al., 2005; Nakamura-Messenger et al., 2006; Garvie et al., 2008).

Here we expand on earlier efforts to investigate the IOM in the Tagish Lake CC. We follow up on SIMS measurements, which showed that the Tagish Lake CC retains primitive IOM (Busemann et al., 2006b) despite having sustained the effects of parent-body alteration (e.g., Nakamura et al., 2003). Thus, the study of this material presents an opportunity to gain insight into questions about the origin and processing of IOM. For example, is the isotopically enriched IOM associated with specific minerals? Did IOM contribute to the products of parent-body alteration? Is there a specific carrier phase or molecule of the isotopic anomalies? We combine site-specific extraction and spatially high-resolution analytical techniques to investigate the isotopically enriched IOM *in situ* rather than as extracts or separates. Our goal is to understand the isotopic composition, mineral associations, and character of the IOM in its original context to gain insight into these questions.

2. SAMPLES AND ANALYTICAL METHODS

We report new results on four small fragments of the Tagish Lake CC for which we previously reported isotopic data (Busemann et al., 2006b). Briefly, individual 5- to 20-μm fragments were hand-picked from a sample of Tagish Lake powder and pressed into clean Au foils for SIMS analysis. It is not known whether the sample originated from the carbonate-rich, -poor, or CM1 lithologies (e.g., Zolensky et al., 2002), though we infer below that these fragments probably came from the carbonate-rich lithology, owing to the abundance and composition of carbonate. We believe that the sample was collected several months after the fall, and so we cannot completely rule out some interaction with lake water. Nonetheless, the survival of isotopically anomalous organics indicates that such interaction, if it occurred at all, was limited.

All fragments were measured for D/H and C/H ratios with the Carnegie Institution's Cameca ims-6f ion microprobe and a subset for C and N isotopic compositions with the Cameca NanoSIMS 50 ion microprobe at the Max Planck Institute for Chemistry in Mainz. Experimental details can be found in Busemann et al. (2006b). Following the D/H imaging measurement, we used a JEOL 6500F scanning electron microscope (SEM) at Carnegie to acquire images and, for fragment #2, elemental maps with an EDAX energy-dispersive spectrometer (EDS). For our purposes, it is important to note that the H isotopic images have a spatial resolution of 1–1.5 μm (based on the primary ion beam size in the ims-6f), compared to 100–150 nm for the NanoSIMS C and N measurements. The size of the D

hotspots could, therefore, be smaller and the D/H ratios much higher than they appear in the isotopic maps. It is also likely that smaller grains containing isotopically anomalous D were missed because they were averaged out by the material surrounding them. Moreover, the difference in spatial resolution between the ims-6f and the NanoSIMS leads to difficulties in aligning the isotopic maps from each of these instruments with each other and with secondary electron images of the fragments of Tagish Lake material. These differences in spatial resolution ultimately lead to some ($\leqslant$1 μm) uncertainty in the exact location of the isotopically anomalous material, but we have been careful to section the hotspots as precisely as possible.

We used an FEI Nova 600 focused-ion-beam scanning-electron microscope (FIB-SEM) at the Naval Research Laboratory (NRL) to make electron-transparent cross sections (typically 10 μm wide) of four matrix fragments extracted from the Tagish Lake CC in order to investigate the minerals and organic matter associated with the isotopic hotspots and gain insight into their character. A 1- to 1.5-μm thick layer of Pt was deposited on all fragments, transecting the isotopically anomalous regions, in order to mitigate ion implantation and radiation damage in the areas of interest. One grain (fragment 2) was extracted *ex situ* and placed on a C-coated TEM grid. The other three grains were prepared using standard FIB techniques (e.g., Pt strap deposition, stair-step profiles), extracted with a micromanipulator, and ion milled to electron transparency ($\sim$100 to 150 nm) inside the FIB using previously described methods (Zega et al., 2007). We note that SIMS is a destructive technique and it is possible for the isotopically anomalous material observed by SIMS to be sputtered away prior to attempts to extract it with the FIB. The amount of material removed in our SIMS measurements here is impossible to estimate since each measured grain experienced a different ion dose and different materials have different sputtering rates. However, we have confidence that some of the isotopically anomalous material survived in our grains because the final measurement cycles of the SIMS measurements showed no signs of declining signals. Moreover, for the two grains with NanoSIMS measurements, the ^{12}C images appear quite similar to those from the ims-6f measurements, once the former images are degraded to the ims-6f spatial resolution. This implies that the organic matter present in the D/H measurements remained during the C and N measurements.

Ion-beam milling is also a destructive process that can result in radiolysis and knock-on damage to the surface of the sample. Damage can be of particular concern for low-Z materials such as organics and its effects on both the faces and the top edge immediately below the Pt strap should be considered. Because these sections were extracted using a 30 kV Ga^+ ion beam, there is a Ga^+ implantation damage layer of 10–30 nm on each of the faces of the sections in which the structure of crystalline materials is disrupted. This surface structural damage does not preclude high-resolution imaging or diffraction analysis of the interior pristine material unless the thickness of the pristine material is less than that of the surface damage. For this reason, sections thinner than 100 nm are not attempted without lowering the Ga^+ beam voltage. In general, the elemental composition of such sections are preserved to within 5 nm of the surface, except for the addition of Ga. Preferential sputtering and re-deposition of sputtered material can alter the composition of the last few nm's of the section faces. The thickness of the FIB section in the TEM observation direction is 100–150 nm. Neglecting Ga, the ratio of compositionally unaltered to altered material to surface is therefore, >9:1, i.e., $>(100-5-5)/(5+5)$, and so the signal from the unaltered material dominates any acquired EDS or EELS spectra. The portion of the FIB section closest to the Pt strap can also sustain damage by the ion beam during deposition of the protective Pt (or other materials such as C) strap. However, under standard operating conditions, Pt typically coats the surface before significant damage can occur. Moreover, the $\sim$16 keV Cs^+ beam used in the original SIMS measurements will induce damage in the top tens-of-nanometers of the sample, making any subsequent damage from the FIB negligible. We have prepared FIB sections of several IOM residues this way and have successfully preserved and analyzed the material at the surface of the section, including nanoglobules (Busemann et al., 2006a, 2007). We note that fragile organic materials, such as polyacrylamide, are more sensitive to electron beam rather than ion beam damage (Bassim et al., 2010). Our experience suggests that surface damage is not a significant concern for interpreting the data of the FIB sections that we report on here.

All FIB sections were examined at NRL with a 200 kV JEOL 2200FS transmission electron microscope (TEM) equipped with an energy-dispersive spectrometer (EDS), in-column electron energy-loss spectrometer (EELS), and bright- and high-angle annular dark-field (HAADF) scanning TEM (STEM) detectors. The compositions of individual grains and regions of interest (ROI) were measured using a thin-window Thermo Electron EDS detector and processed with Noran System Six software. Illumination conditions and acquisition parameters (scanning vs. imaging mode, spot size, condenser aperture, convergence angle, time constant, and integration time) were varied based on the size of the ROI and adjusted to optimize counting statistics. EELS was used to evaluate C chemistry on select ROIs. Spectra were collected in either image (converged beam) or STEM mode at 200 keV from regions measuring $\sim$1 to 100 nm in diameter using 3–10 s acquisition times. Some experiments were performed with a lowered emission current (by decreasing the A1 extraction voltage in the field-emission gun), which provided an energy resolution of $\leqslant$1 eV as measured from the full width at the half-maximum height of the zero-loss peak (ZLP). Both the C K core-loss edge and low-loss spectra (including both the ZLP and plasmon peaks) were acquired at all ROIs. Spectral processing included background subtraction in the form of AE^{-r} (Egerton, 1996), removal of plural scattering effects (Fourier-ratio method), and alignment and summation of offset spectra to improve the signal-to-noise ratio. Some spectra were numerically smoothed using a 1- to 1.5-eV wide window to average out the noise variations without adding any spurious artifacts. Selected-area electron-diffraction (SAED) patterns were acquired, where

possible, to aid in the identification of unknown phases. All patterns were measured manually (in Photoshop) and using crystallographic image-processing software (Hovmöller, 1992) based on calibrated camera constants. The indexing of the SAED patterns was based on comparison to appropriate reference structures, and some were additionally verified with calculated patterns using JEMS multislice (Stadelmann, 1987) and SingleCrystal software packages.

Selected FIB sections were taken to the National Synchrotron Light Source (NSLS) at Brookhaven National Laboratory and were measured with the scanning transmission X-ray microscope on the X1A beamline. Image stacks were acquired over an energy range of ~280 to 320 eV to evaluate the X-ray absorption near-edge structure (XANES) at the C K edge to further assess C chemistry. We used a 0.3-eV energy step and 1 ms integration time for all stacks except in the fine-structure region of the near-edge (283.5–292 eV) where we used 0.1 eV energy steps and a 2 ms integration time.

We note that pinpointing the carrier of isotopic anomalies *in situ*, whether it be a distinct grain, phase, or molecule, is a challenging task. It is important to keep in mind that SIMS is a surface technique that provides information about where *on* the sample the isotopically enriched material occurs. Although spatial correlations among isotopic maps provide information on the composition of the carrier and some insight into its nature, we have no additional information on its characteristics or spatial associations without investigation at higher spatial scales. Because of the disparity in resolution between the SIMS instruments (1 μm for the ims-6f, 100 nm for the NanoSIMS) and the TEM (down to the atomic), i.e., because we cannot make isotopic measurements on the scale at which we can make TEM observations, we need to characterize the microstructure of *all* of the material that occurs in the regions of the FIB sections corresponding to the isotopic hotspots as measured by SIMS. The data in the text below reflects this need, and we attempt to infer from them the carrier(s) of the isotopic anomaly.

3. RESULTS

Although all fragments were measured for their isotopic compositions, for the sake of brevity, we show the complete isotopic maps only for the first of the four fragments described. However, we indicate the location of the isotopic hotspots on secondary electron images of each of the other three fragments.

3.1. Fragment 1

SIMS analysis reveals isotopic heterogeneity in a 15-μm wide particle, with prominent, spatially uncorrelated D and ^{15}N hotspots (Fig. 1). The ~500-nm diameter ^{15}N hotspot ($\delta^{15}N = 1020 \pm 140‰$) occurs near to the top of the particle (Fig. 1e), whereas the ~2 μm diameter D hotspot ($\delta D = 2800 \pm 400$ ‰) occurs below and to the right of center (Fig. 1d). The D hotspot is clearly correlated with C in the ims-6f ^{12}C image (Fig. 1b). However, the higher-resolution NanoSIMS ^{12}C image reveals numerous small C-rich regions in the vicinity of the D hotspot (Fig. 1c), any one (or more) of which could be associated with the D anomaly. This illustrates the difficulty of aligning images acquired with varying resolutions and also suggests that the true D-enrichment of this material is likely much higher than measured. We prepared an electron-transparent cross section of the fragment, transecting the ^{15}N and D hotspots (dashed-white line in Fig. 1a–e). The ambiguity of the true size and location of the D enrichment due to the relatively coarse resolution of the D/H measurement means that we cannot be sure that the FIB slice contains the D-rich material. Nonetheless, it certainly contains material that was situated very closely to the anomalous material in the meteorite. We are confident that the FIB slice does contain material from the ^{15}N hotspot. Bright-field TEM imaging reveals a mixture of fine- and relatively coarser-grained material occurs in the regions of both the ^{15}N and D hotspots (Fig. 1f), and the variable contrast in HAADF images shows that there is also a wide range in the average atomic number (Z) (Fig. 1g). Many of the brighter grains are sulfides that occur throughout the fragment.

The first 500 nm of the FIB section, measured from the left edge, corresponds to the region containing the ^{15}N anomaly (Fig. 2a). High-resolution TEM (HRTEM) imaging shows that some of this material is amorphous, particularly that closest to the left edge of the FIB section (Fig. 2b). However, crystalline material also occurs within and near to the ^{15}N-rich region, and HRTEM imaging shows layered structures containing 0.7-nm periodicities (Fig. 2c and d). EDS measurements from selected areas across the ^{15}N-rich region indicate Fe, Mg, Al, Si, O, and C are the major constituents (cf., Fig. 3a and b).

The HRTEM and EDS data are consistent with serpentine and a C-bearing material. The left-most edge of the FIB section is rich in C and shows a high C/O ratio. The C/O ratio decreases from left to right across the hotspot as serpentine becomes more abundant, but C remains in the EDS spectra throughout the region, suggesting a nanoscale intergrowth of organic and serpentine material. The serpentine occurs along much of the length of ^{15}N-rich region and in some areas extends from the Au substrate to the Pt strap (cf., Fig. 2a, c and d). Some of this material exhibits chrysotile-like terminations, i.e., the (0 0 1) layers (lattice fringes separated by 0.7-nm) show a slight amount of radial curvature (Fig. 2c). The energy-loss near-edge structure (ELNES) of the C in the ^{15}N-rich region reveals a peak at 285 eV followed by a delayed maximum at ~297 eV, consistent with the reference spectrum acquired from amorphous C (Fig. 3c). This structure is due to electronic transitions from 1s to π^* and σ^* antibonding orbitals and is characteristic of C=C in aromatic units (see Egerton, 1996 and references therein). EELS measurements at the N K edge were attempted, but no significant edge intensity was observed.

The area approximately 4.9 μm away from the left edge of the FIB section, corresponding to part of the D hotspot, contains a mixture of coarse- and fine-grained material showing a range of Z-contrast (cf. Fig. 1f and g). Part of the Pt was eroded during *in situ* milling, dividing the ~2.7 μm wide region that corresponds to the D anomaly

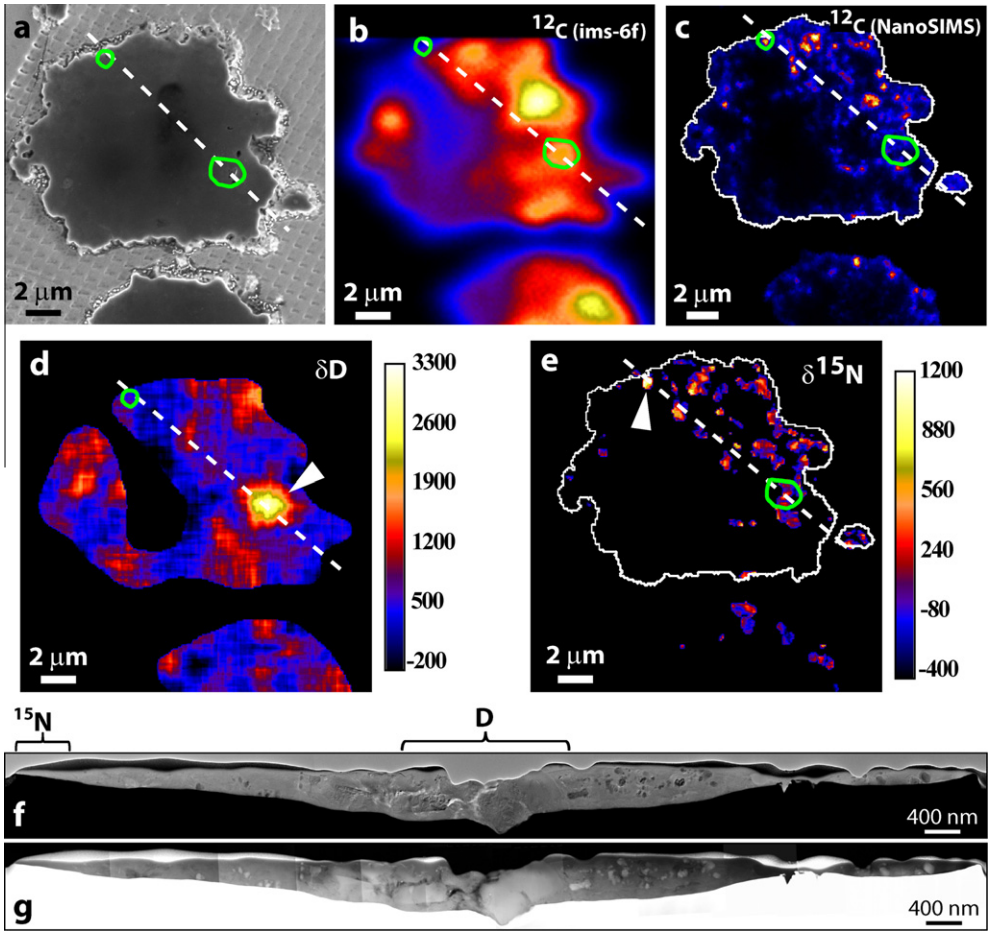

Fig. 1. SIMS and TEM data for Tagish Lake matrix fragment 1. (a) Secondary electron image showing the grain after SIMS analysis but prior to FIB sectioning. Here and in other fragments, the surface appears smooth because of the ablation of material by the primary ion beam of the SIMS. (b) Abundance map of C measured in the ims-6f, shown as counts. (c) Abundance map of C measured in the NanoSIMS 50, shown as counts. (d) D/H isotopic ratio map as measured by the ims-6f ion microprobe. (e) N-isotopic ratio map as measured by the NanoSIMS 50. The dashed-white lines indicate the location of the FIB transect. The white arrowheads and green circles indicate the locations of the isotopic hotspots. The scale bars on the right of (d) and (e) denote the magnitude of the delta value relative to SMOW. (f) Bright-field and (g) HAADF TEM image mosaics showing the overall FIB section (ROI surrounding hotspots is indicated by brackets above (f).)

into two areas (hereafter, left and right) that contain preserved straps (Fig. 1f, bracket). Bright-field imaging of the left side shows an area with uniform contrast beneath the Pt strap, and SAED and HRTEM reveal that this area is amorphous (Fig. 4a). Two large (hundreds of nm) grains occur beneath the amorphous material and exhibit varied degrees of diffraction contrast (labeled '1' and '2' in Fig. 4a). SAED patterns show that these grains are crystalline, and measurements on diffraction patterns obtained in multiple orientations and HRTEM images (Fig. 4b–d) are all consistent with a rhombohedral carbonate structure. Measurements suggest several dolomite-group phases (dolomite, ankerite, and kutnohorite) are consistent with grain 1, and SAED simulations based on the dolomite structure provide a plausible match to the experimental pattern. Measurements of the SAED pattern acquired from grain 2 suggest calcite or dolomite-group phases, and simulations of [0 0 0 1] zone-axis patterns also provide plausible matches to the experimental data. However, EDS analysis shows that these grains are not pure endmembers but rather contain significant Fe and Mg with lesser amounts of Ca and Mn, indicating that these are mixed-cation carbonates, qualitatively consistent with carbonates observed in the carbonate-rich lithology (Zolensky et al., 2002).

HAADF imaging shows that the amorphous region closest to the Pt strap has uniform contrast and that it is darker than the carbonate grains (Fig. 5a), indicating it has a lower average Z. Parts of the carbonate grains show areas of dark patchy contrast ($\leqslant$20 nm wide) in the HAADF images that correlate with areas of lighter contrast in the bright-field images, suggestive of lower-density than the bulk carbonate. The carbonate grains have an otherwise uniform intensity in the HAADF image, indicating a uniform composition, except for an area in the top-left part of the lower grain that shows slightly higher Z-contrast. EDS analysis reveals that both the amorphous material and the carbonates contain Mg, Fe, Ca, Mn, O, and C, but the amorphous region contains

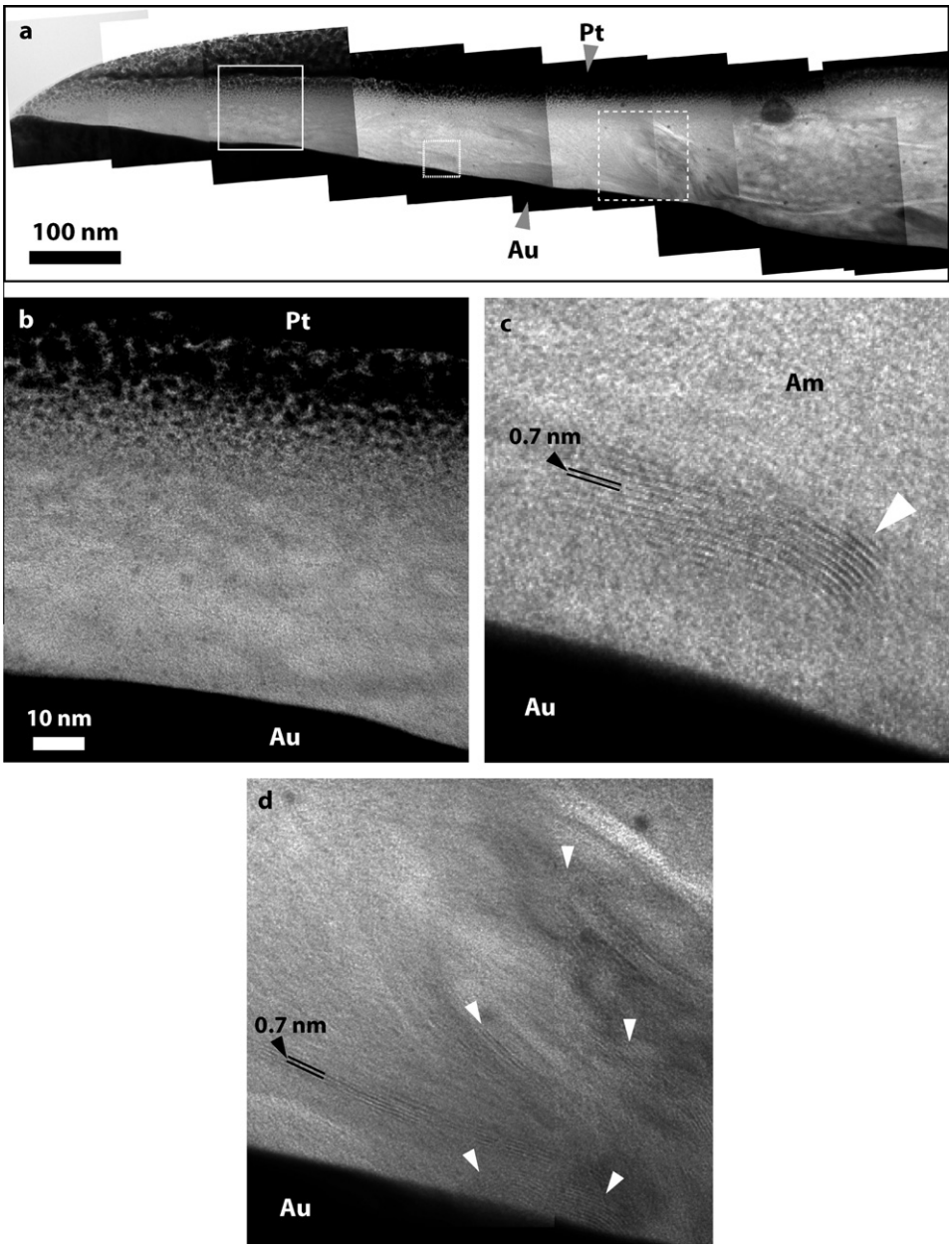

Fig. 2. Structural data from the ^{15}N-rich region of fragment 1. (a) Bright-field TEM image mosaic of overall region. The Tagish Lake material occurs between the Pt strap and Au substrate. (b) Bright-field image from white-boxed area in (a). There is a slight gradation at the top of the FIB section due to re-deposition of Pt during *in situ* milling. (c) HRTEM image of small, dashed-white box in (a). The serpentine grain has a chrysotile-like termination (white arrowhead) and is surrounded by amorphous (Am) material. (d) HRTEM image of large, dashed-white box in (a). Serpentine grains (arrowheads) occur throughout this region.

significantly more C than the carbonates (Fig. 5b, cf., spectra 1, 2, and 5). The C-ELNES in the amorphous region (Fig. 5c, spectrum 3) is consistent with the reference spectrum from amorphous C (Fig. 5c, AC), indicating abundant aromaticity. In comparison, the C-ELNES of the top-most carbonate grain (Fig. 5c, spectrum 4) exhibits similarities to the reference spectra acquired from several of the pure C allotropes with peaks at 285, 290, and 292 eV followed by a minimum near 301 eV. This near-edge structure indicates abundant carbonate bonding (peaks at 290 and 292 eV) with some aromaticity (285 eV) and the possibility of sp^3 diamond-like character (minimum near 301 eV), but we could not confirm the latter with SAED patterns or HRTEM imaging. The EELS spectrum from the bottom carbonate (Fig. 5c, spectrum 5) shows a pronounced peak at 290 eV followed by smaller peaks at ~296 and ~301 eV, consistent with the reference spectrum acquired from amorphous C and calcite, indicating a minor amount of aromaticity and abundant carbonate bonding.

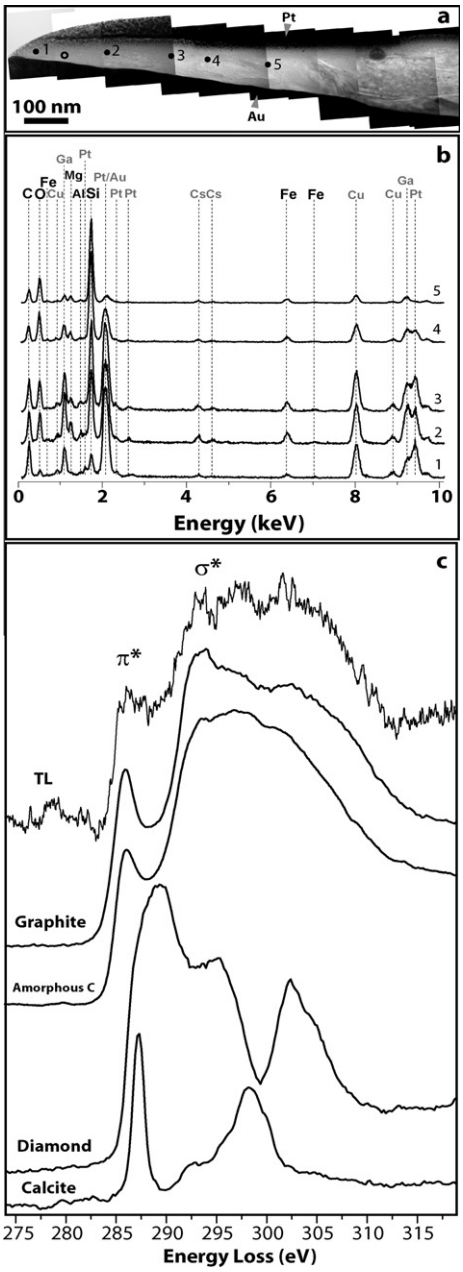

Fig. 3. Compositional data from the ^{15}N-rich region of fragment 1. (a) Bright-field TEM image mosaic of overall region showing the location of compositional measurements. (b) EDS data acquired from ^{15}N-rich region. The spectra are numbered and correlate to the positions (filled circles) in (a). Ga occurs in the spectrum due to implantation from the FIB; Cs from the SIMS. The Cu peak is from the support used to hold the FIB section. Pt and Au are from the strap and substrate, respectively. (c) C K EELS spectrum (top) acquired from the ^{15}N-rich Tagish Lake (TL) material (area indicated by the open circle in (a)) shown with spectra acquired from phase-pure standards.

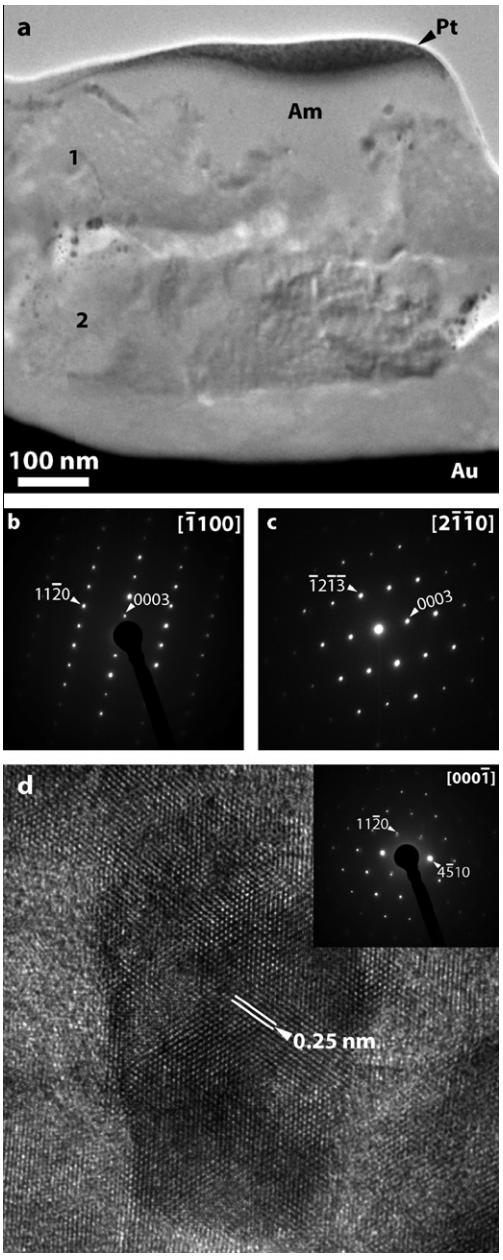

Fig. 4. Structural data from the left side of the C-enriched and D-rich region of fragment 1. (a) Bright-field TEM image showing amorphous (Am) material and carbonate grains (labeled '1' and '2'). (b and c) SAED patterns acquired from grain '1'. (d) HRTEM image and SAED (inset) from grain '2' showing some localized disorder. The *d*-spacings measured from these patterns are close to several of the endmember carbonates, but the indexing is based on simulations fit to the experimental pattern. Calculated patterns for the dolomite structure provided a best fit to the experimental patterns shown in (b) and (c), whereas calcite provided a best fit to that shown in (d).

Bright-field imaging on the right side of the D hotspot reveals a large (~1 μm wide) grain (Fig. 6a, white arrowhead) that SAED shows is crystalline (Fig. 6b and c). Measurements on patterns from multiple orientations are also consistent with a rhombohedral carbonate structure. EDS shows that this grain contains abundant Fe and Mg with minor Ca and Mn, and so it is also clearly a mixed-cation carbonate, qualitatively similar in composition to previous measurements of carbonates in the Tagish Lake CC (Zolensky et al., 2002). Simulations of SAED patterns of

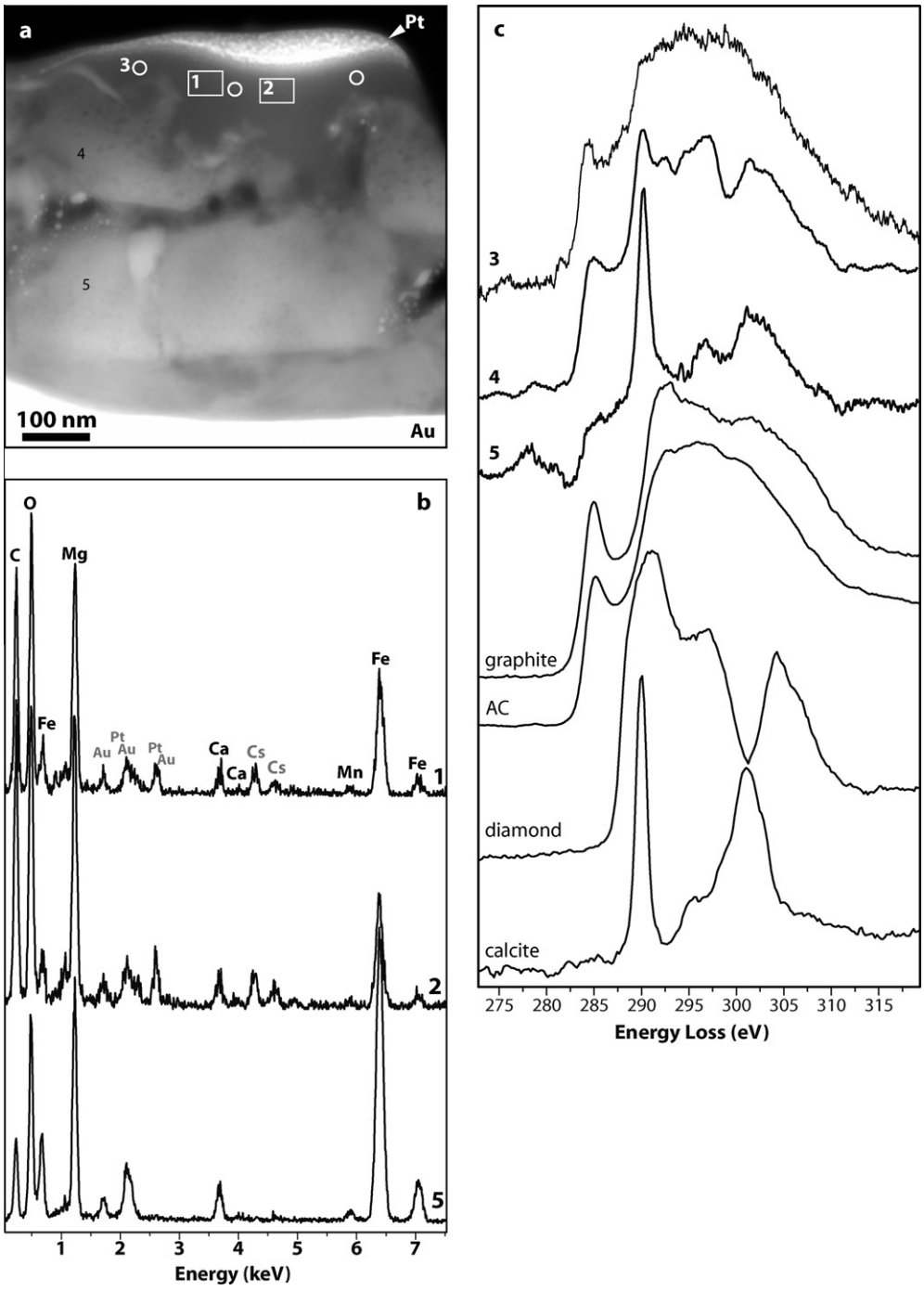

Fig. 5. Compositional data from the left side of the C-enriched and D-rich region of fragment 1. (a) STEM-HAADF image showing the carbonate grains and amorphous material. (b) EDS spectra numbered according to the area from which they were acquired in (a). Pt and Au are from the strap and substrate, respectively. (c) C K EELS spectra shown together with spectra acquired from phase-pure standards, labeled according to where they were acquired in (a). Spectrum '3' is a representative composite spectrum acquired from the areas indicated by the open white circles.

several dolomite-group phases provide plausible matches to the measured data. The region closest to the preserved Pt strap shows uniform contrast (Fig. 6a, white arrowhead with black outline), and HRTEM imaging reveals that it is amorphous (Fig. 6d). The amorphous material has a uniform contrast in the HAADF image suggesting a homogeneous composition (Fig. 7a). The amorphous material and the carbonate both contain Mg, Fe, Ca, O, and C, but the former contains significantly more C than does the carbonate (Fig. 7b). The overall shape of C-ELNES from the amorphous region is similar to that from the reference spectrum of amorphous C, but it has a broader peak at 285 eV

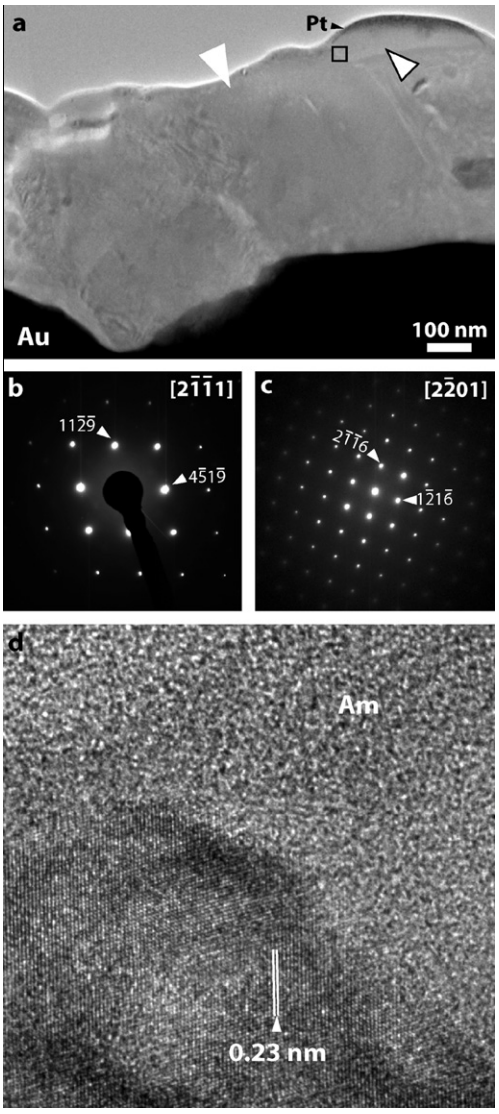

Fig. 6. Structural data from the right side of the C-enriched and D-rich region of fragment 1. (a) STEM-BF image showing carbonate grain (white arrowhead) and amorphous material beneath the Pt strap (white arrowhead with black outline). (b and c) SAED patterns acquired on the carbonate grain in (a) in multiple orientations. As with the grains on the left side, the *d*-spacings measured from these SAED patterns are close to those for several of the endmember carbonate structures. (d) HRTEM image of area within the solid-black box in (a) showing the interface between the carbonate grain and the amorphous material (Am).

(Fig. 7c), suggesting a relatively lower abundance of aromatic C as compared to the left side of the D-rich hotspot. The C-ELNES from the carbonate is consistent with the reference spectrum from calcite, confirming carbonate bonding in this material (Fig. 7c).

3.2. Fragment 2

SIMS analysis of this ~17 × 8 μm fragment reveals two D hotspots (white circles, Fig. 8a), correlated with high C contents (subject to the same caveats discussed above about the spatial resolution of the D/H measurements). The left D anomaly (δD ~1500‰) occurs near the center of the left particle and measures approximately 2.1 μm in diameter. The one on the right occurs near the center-top part of the grain and measures approximately 1.6 μm wide (δD ~3000‰). SEM-EDS maps of this fragment indicate that the right-most D hotspot is spatially correlated with carbonate, based on the presence of Mg, C, and O, but not Si. This fragment was not measured for N isotopes. We deposited a Pt strap that transects the two D hotspots (Fig. 8a).

Bright-field imaging of the left ~3.6 μm of the FIB section shows that this area contains a mixture of fine- (⩽10 nm) and coarse-grained (tens of nanometers to microns) material (Fig. 8b), near to and away from the Pt strap, i.e., both close to and far from the surface analyzed by SIMS. HAADF imaging reveals that both bright- and dark-contrast material occurs in this area as well, indicating large variations in average atomic number. SAED reveals that some of these grains are crystalline. Spot analysis with EDS indicates that the brightest grains in the HAADF image are Fe–Ni sulfides (Fig. 8c and d) interspersed with IOM (darkest contrast) and silicates (moderate contrast). The largest grain in this region, which is closest to the D hotspot, is a ~1-μm wide carbonate that contains a low-*Z* rim on its left-edge (Fig. 8d and inset SAED pattern).

In comparison, the right-most D hotspot occurs approximately 8.9 μm away from the left-most edge of the FIB section. Bright-field imaging shows that this region also contains a mixture of material, but it is finer grained than that corresponding to the D hotspot on the left side of the section (Fig. 8b–e). The material closest to the Pt strap on the left-hand side of the hotspot does not exhibit any discernable grain boundaries and appears solid in the bright-field image (Fig. 8b, area indicated by the right-most dashed line and white arrow). SAED indicates that it is amorphous. HAADF imaging shows that this material has a dark contrast (Fig. 8c and e), indicating, on average, a low-*Z* composition. The low-*Z* material is intermixed with higher-*Z* material toward the right-hand side of the hotspot, and bright-field imaging reveals that some of the material has a fibrous morphology. EDS shows that the material in the hotspot contains abundant C and Si, lesser amounts of O, Mg, and Fe, and minor Al, Ca, and Ni. EELS at the C K edge shows a spectrum similar to amorphous C, i.e., a small peak at 285 eV followed by a delayed maximum, indicating aromatic groups (Fig. 8g). We infer that this is a mixture of fine-grained silicate and organic C. Although it is possible that this thin C-rich layer was deposited in the SEM when acquiring EDS maps, the presence of other elements, e.g., O, Mg, Al, Si, Ca, Fe, and Ni as indicated by TEM–EDS argues against this as does the high C ion signal observed in this region during the initial SIMS measurement.

3.3. Fragment 3

Fragment 3 measures approximately 8.5 × 7.5 μm wide, and SIMS analysis reveals D-rich carbonaceous material (average $\delta D = 650 \pm 150‰$) throughout much of the

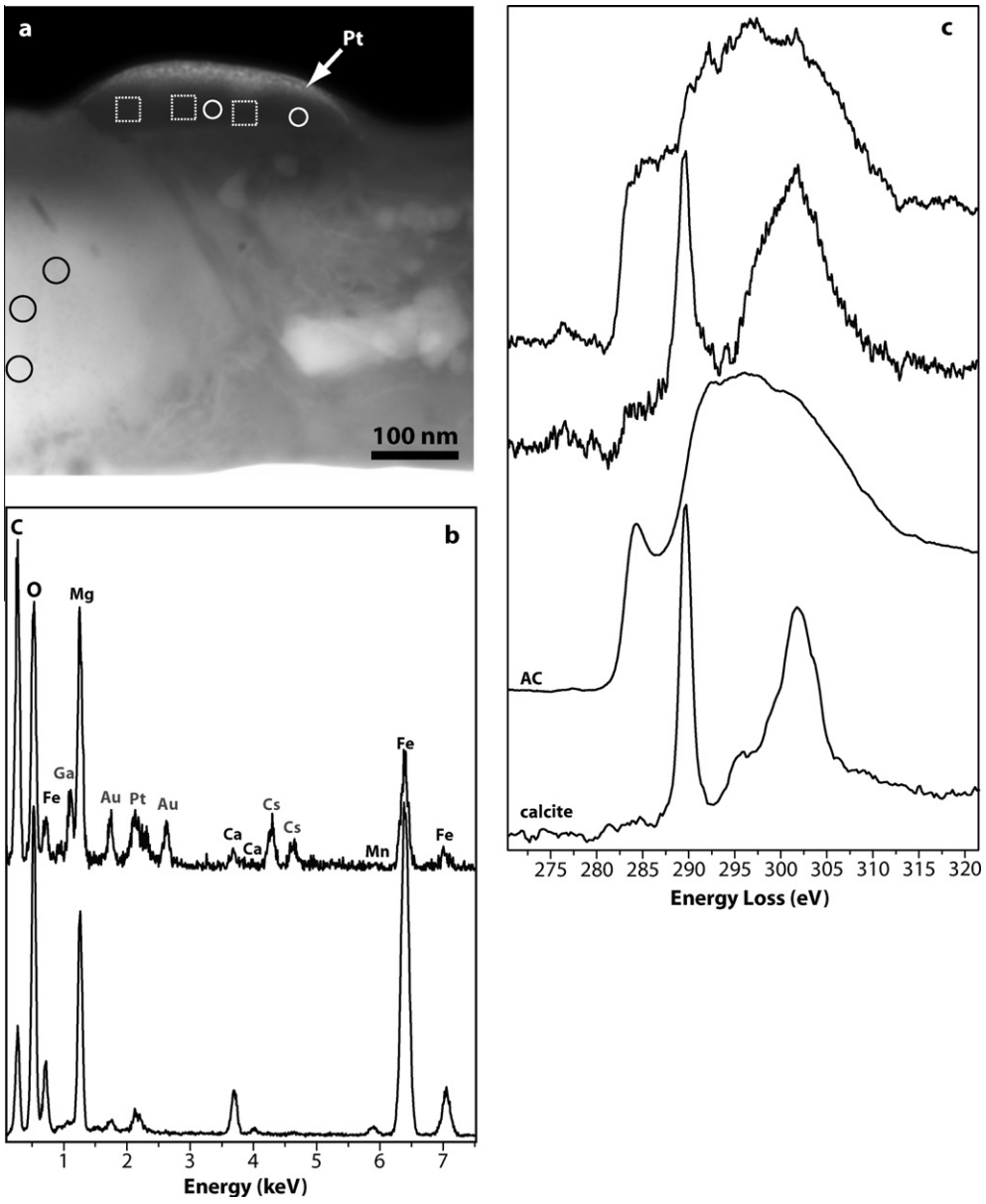

Fig. 7. Compositional data from the right side of the C-enriched and D-rich region of fragment 1. (a) STEM-HAADF image showing the right half of the carbonate grain and the amorphous material beneath the Pt strap. (b) EDS spectra acquired from the amorphous material (top) and carbonate grain (bottom). The top spectrum was acquired in STEM mode and is representative of the areas indicated by the white squares, whereas the bottom spectrum was acquired with a broader parallel beam from most of the grain. (c) C K EELS spectra from amorphous material (top) and carbonate grain (2nd from top) together with reference spectra from amorphous carbon (AC) and calcite. The spectrum for the amorphous material and carbonate are composites of the areas indicated by the white and black circles, respectively.

fragment. A ~1.7 μm diameter D hotspot occurs on the right edge of the grain near to the top (Fig. 9a). Because the apparent size of the hotspot is similar to the spatial resolution of the SIMS images, it is possible that the anomalous material was smaller and more anomalous than the measured δD value of 1400 ± 300‰. NanoSIMS N-isotopic measurements were not made on this sample. We deposited a Pt strap across the top part of the fragment to transect the D hotspot and other less anomalous C material for *in situ* FIB extraction (Fig. 9a).

Bright-field and HAADF images of the FIB section reveals a fine-grain mixture of material in the areas corresponding to the D anomaly (black arrow between Fig. 9b and c). There are several grains in the area corresponding to the D hotspot, i.e., the right-most 2.0 μm of the FIB section, that show up readily in the bright-field image due to their dark diffraction contrast. The corresponding HAADF image reveals that these grains have bright contrast relative to their surrounding material, indicating high average Z, and EDS analysis on several of them reveals prominent

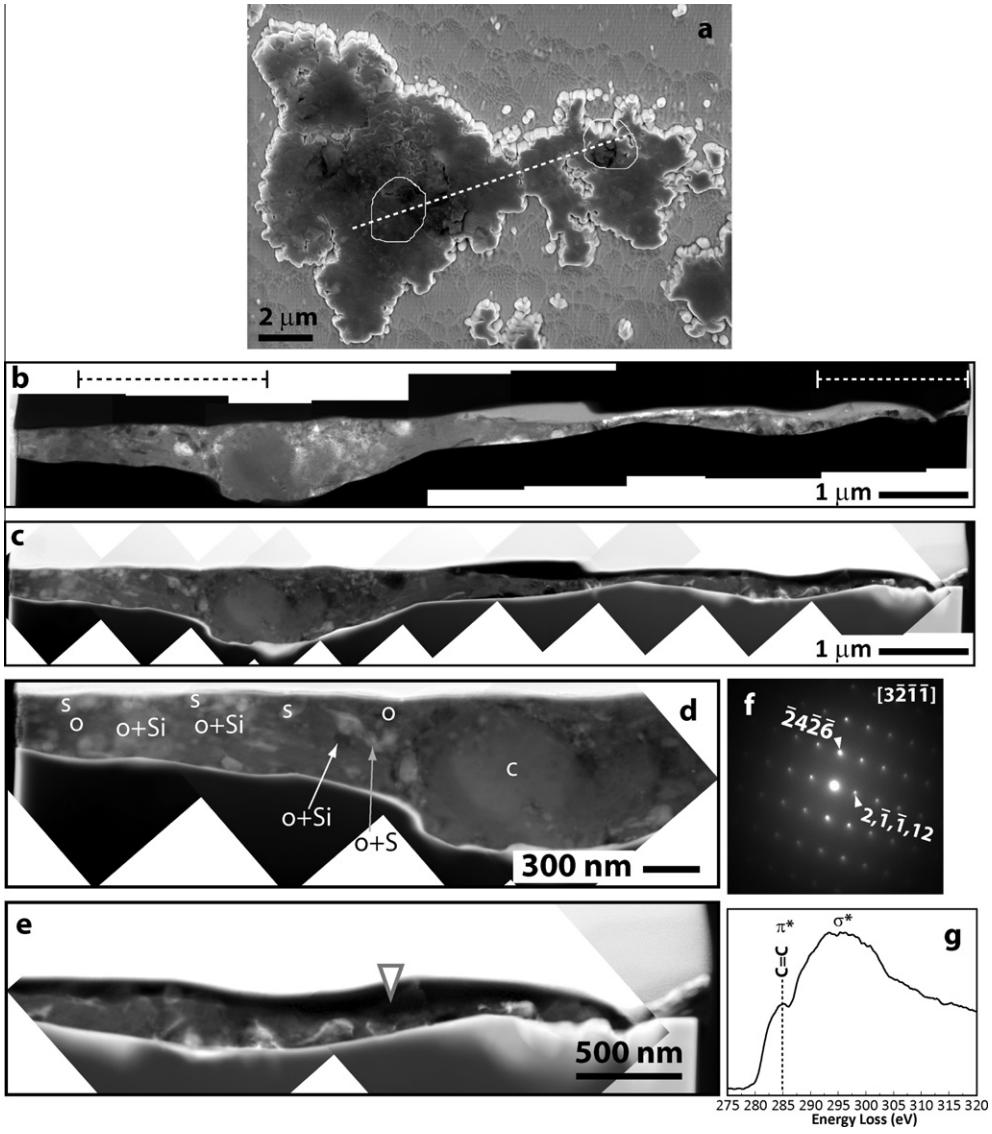

Fig. 8. SIMS and TEM results on fragment 2. (a) Secondary electron image showing the locations of the D hotspots (white circles) and the location of the FIB cross section (dashed-white line). (b) STEM-BF image showing overall FIB section with areas corresponding to the D hotspots indicated (dashed lines above the image and white arrow). (c) STEM-HAADF image of the overall FIB section. (d and e) STEM-HAADF images showing enlargements of the hotspot regions indicated in (b). Organic (O) material, silicates (Si), and sulfides (S) occur with carbonate (C). (f) SAED pattern acquired from carbonate grain in (d). (g) C K EELS spectrum acquired from the area indicated by the white arrowhead in (e).

Fe, Ni, and S peaks. SAED patterns show that these grains are crystalline, but their small sizes ($\leqslant$100 nm) precluded single-crystal zone-axis patterns from being acquired, thus making precise phase identification difficult. Nonetheless, measurements from an SAED pattern acquired from one of the grains are consistent with pentlandite or pyrrhotite, and so we refer to these grains as Fe–Ni sulfides. The sulfides are surrounded by a much finer-grained material ($\leqslant$10 nm) exhibiting a relatively darker contrast in the HAADF image (Fig. 9c). Much of the fine-grained material lacks clearly defined grains and some of it appears to be porous. However, localized areas contain fibrous morphologies suggestive of sheet silicates (Fig. 9b and d white arrowheads with gray outline). EDS shows that the fine-grained material contains Fe, Si, Mg, O, and C, suggesting a fine-grained silicate mixture with C-bearing material. Adjacent to one of the sulfides is a 200 nm wide euhedral grain with *Z*-contrast that is intermediate between the fine-grained material and the sulfides (Fig. 9c, black arrowhead). EDS analysis on this grain shows that it contains abundant C, O, Fe, and Mg with minor Ca and Mn. Measurement of an SAED pattern acquired from it is consistent with rhombohedral carbonate (Fig. 9d) and together with simulations provide a close match to magnesite.

We acquired X-ray absorption spectra from this FIB section. Principal component analysis of image stacks from the entire section, which includes the D-rich and less D-rich material, reveals small peaks at 285, 286.7, 288.9 eV, and a

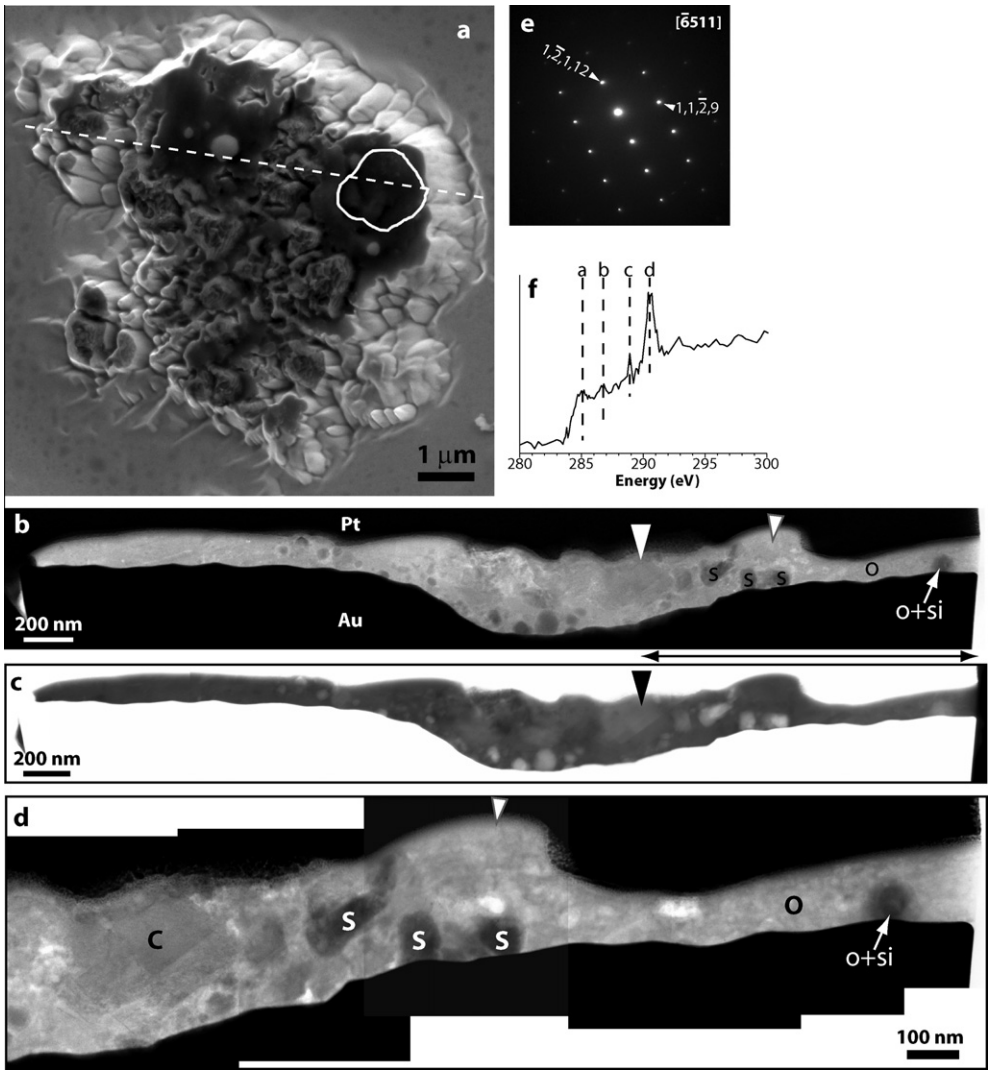

Fig. 9. SIMS and TEM results on fragment 3. (a) Secondary electron image showing the location of the D hotspot (white circle) and that of the FIB transect (dashed-white line). (b) and (c) STEM-BF and -HAADF images, respectively, showing the overall FIB section. Organic (o) material occurs with sulfides (s), carbonate (white arrowhead in b; black in c), and silicates (Si) within the D hotspot (black arrow between b and c). Regions containing fibrous morphologies (white arrowhead with gray outline in b) also occur. (d) Enlargement of area in FIB section corresponding to the D hotspot (black arrow between b and c). Mineral identities abbreviated as above. (e) SAED pattern acquired from the carbonate grain (white arrowhead in b). (f) C XANES cluster spectrum derived from principal component analysis of the entire image stack, which includes the D hotspot and less D-rich material. Peaks 'a–d' are assigned to aromatic, vinyl-keto and/or nitrile, carboxyl, and carbonate functional groups, respectively.

major peak at 290.5 eV (peaks 'a–d', respectively, Fig. 9e). These absorption energies can be assigned to aromatic, vinyl-keto and/or nitrile, carboxyl, and carbonate functional groups based on comparisons with reference spectra (e.g., Cody et al., 2008; Hitchcock and Mancini, 1994). Although the region of the FIB section containing the D hotspot proved somewhat thick (>100 nm) for XANES measurements, we were able to observe broad absorption features at 285 and 290 eV, consistent with aromatic and carbonate functional groups.

3.4. Fragment 4

Fragment 4 measures approximately 6.5 × 10.3 μm and contains spatially heterogeneous C-rich areas. Whereas the average δD value for the fragment is ~500‰, a D hotspot with δD 1300 ± 300‰ is apparent along the right-hand side of the sample (Fig. 10a). This hotspot measures ~1.5 μm wide, comparable to the spatial resolution of the measurement, and is associated with a strong C concentration in the ims-6f image. Comparison of the ims-6f images with the higher-resolution NanoSIMS images reveals that there are several C-enriched sub-μm regions in the general area of the D hotspot. Unfortunately, it is not possible to unequivocally determine which is associated with the D anomaly. The fragment also shows a moderate bulk ^{15}N anomaly with $\delta^{15}N = 55 \pm 9‰$, with one sub-region showing a significantly higher enrichment. This ~300 nm diameter hotspot ($\delta^{15}N = 515 \pm 170‰$) occurs on the left-most edge about midway from the bottom (Fig. 10a). We

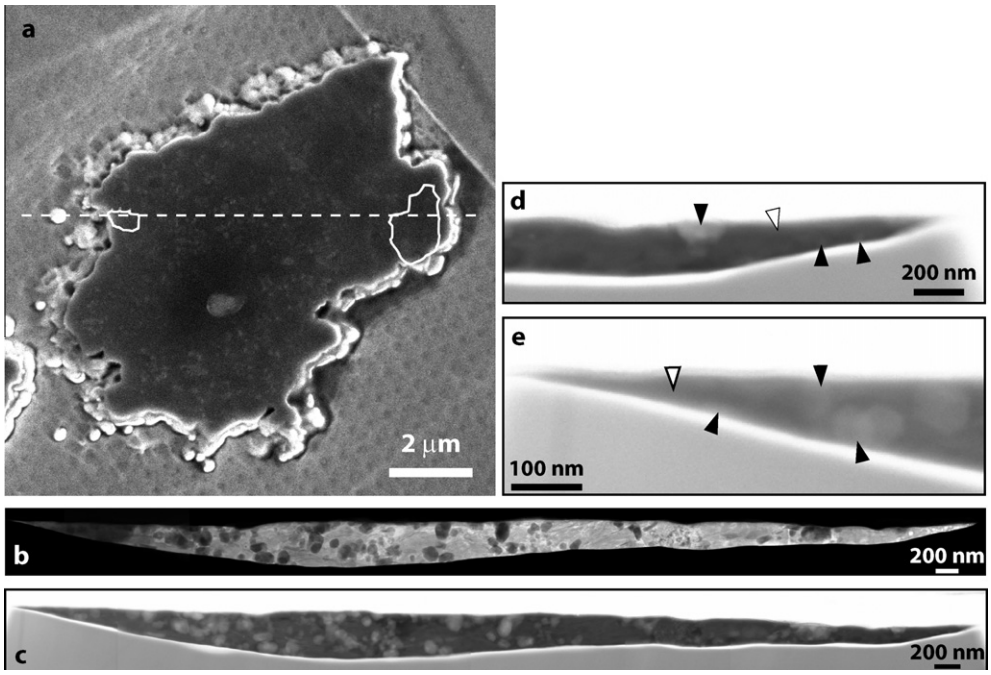

Fig. 10. SIMS and TEM results on fragment 4. (a) Secondary electron image showing the location of the D and ^{15}N hotspots (right and left white polygons, respectively) and that of the FIB cross section (dashed-white line). (b) STEM-BF and (c) STEM-HAADF images of the overall FIB section. (d) STEM-HAADF image of the area containing the D hotspot. Fe–Ni sulfides and Fe–Mg silicates (black arrowheads) occur intimately mixed with fine-grained silicate and C-bearing material (white arrowhead). XANES measurements indicate that some of this C-bearing material is carbonate. (e) STEM-HAADF image of the region corresponding to the ^{15}N hotspot. Coarse, high-Z grains indicated by the black arrowheads; low-Z material by the white arrowhead.

deposited a Pt strap transecting the ^{15}N and D hotspots and prepared an electron-transparent cross-section in the FIB for higher-resolution investigation.

The right-most 1.5 μm of the FIB section, which corresponds to the area containing the largest D anomaly, contains several grains exhibiting moderate diffraction contrast (Fig. 10b). The grains range in size from $\sim$ 10 to 50 nm and are surrounded by finer-grained material. Although the diffraction contrast of these grains suggests that they are crystalline, their small size precludes phase identification using SAED patterns. However, they exhibit bright contrast in the HAADF image relative to the finer-grained material surrounding them, suggesting average higher Z (Fig. 10d, black arrowheads). STEM-based EDS measurements indicate that these grains are Fe–Ni sulfides and Fe–Mg silicates. The fine-grained material surrounding the silicates and sulfides (Fig. 10d, white arrowhead) contains Fe, Ni, Mg, Si, O, and C, suggesting a fine-grained mixture of silicates and C-bearing material. The thickness of this FIB section (>100 nm) and the proximity of the hotspots to the Pt strap and the Au substrate made XANES measurements challenging. Many spectra had low signal-to-noise or their intensities were close to saturation, or some combination of these two. Nonetheless, a composite C XANES spectrum from the region corresponding to the D hotspot does reveal a peak at 290 eV, indicating carbonate bonding in this region. It also contains a subtle feature at 287.5 eV, suggesting the possibility of aliphatic functional groups, but this could not be confirmed.

The left-most 300 nm of the FIB section, including the ^{15}N hotspot, contains fine-grained low-Z material with no discernable grain boundaries (Fig. 10e, white arrowhead) intermixed with higher-Z coarser (tens of nm) grains (Fig. 10e, black arrowheads) containing moderate diffraction contrast (cf., Fig. 10b, c and e). The diffraction contrast suggests that the coarser grains are crystalline, but as with those on the right side of the FIB section, they were too small for phase identification by SAED. STEM-based EDS measurements shows that one of the high-Z grains contains Fe, Si, Mg, O, and C, whereas another contains Fe, Ni, S, Si, Al, Mg, O, and C. The data suggest that there is a mixture of phases in this region, probably some combination of silicates, sulfides, and C-bearing material (either organic or carbonate). In comparison, the lower-Z material contains more abundant C than the higher Z coarse grains. XANES measurements of the FIB section in this ^{15}N-rich region shows a broad absorption feature beginning at 285 eV, but the intensity in the spectrum saturates shortly after edge onset, thus precluding precise assignment of functional chemistry.

4. DISCUSSION

Although D and ^{15}N do not always correlate in the same grain, their correlation with C enrichments suggests that they are contained within an organic carrier. Previous work has shown that some of the IOM in the Tagish Lake CC is composed of discrete spherical grains. These nanometer-sized

hollow spheres (nanoglobules) are distributed in the matrix and can contain anomalies in N and H isotopes (Nakamura et al., 2002; Garvie and Buseck, 2004; Messenger et al., 2004; Ashley et al., 2005; Nakamura-Messenger et al., 2006; Garvie et al., 2008). HRTEM of the nanoglobules shows that they are amorphous and EELS measurements reveal a molecular structure with abundant aromaticity (Garvie and Buseck, 2004; Nakamura-Messenger et al., 2006). Although we find that much of the isotopically anomalous organic material in these Tagish Lake fragments is amorphous and contains a high degree of aromaticity (e.g., Figs. 3c, 5c, 7c, 8f, 9e), we have not observed nanoglobules, which may be due to their low abundance in this meteorite (Nakamura-Messenger et al., 2006). However, most nanoglobules would not be recognizable at the coarse resolution of the ims-6f H-isotope images, and we therefore cannot rule out that some of the observed anomalies were originally carried by them (e.g., Fig. 2b of Busemann et al., 2006b). The isotopically anomalous material in these FIB sections of the Tagish Lake fragments appears porous or solid (Figs. 5a, 7a, 8b, 9b, 10d and e). We have observed both solid and porous forms of IOM, containing abundant aromatic character, in FIB sections of the GRO 95577 CR1 meteorite (Busemann et al., 2007). The variations in the morphology of the organic component from these Tagish Lake fragments, as well as its short-range order and abundant aromaticity, are consistent with previous observations on IOM residues. We therefore infer that the organic material in these fragments is likely similar to IOM except that we are observing it intimately mixed with other materials *in situ* rather than in concentrated residue form. The organic material is almost certainly the carrier of the observed ^{15}N enrichments and also a very likely carrier of the D anomalies. However, as we discuss below, the complex intergrowths do not preclude inorganic phases as being possible carriers of the D anomalies as well. Nevertheless, the morphological heterogeneities of the IOM suggest that either there was a range of pathways for its formation, it experienced varied parent-body histories, or some combination of the two. The isotopic composition of the IOM also suggests complex formation and alteration histories.

Earlier efforts to characterize the origin of IOM in different types of planetary materials have revealed that some of it has primitive origins. For example, Robert and Epstein (1982) and Yang and Epstein (1983) measured bulk residues of carbonaceous chondrites and showed that they could contain highly enriched organic matter ($\delta D \leqslant 10{,}000‰$), and based on the magnitudes of the anomalies, suggested that such material likely originated in interstellar clouds via ion-molecule reactions at low temperatures (<150 K). Messenger (2000) later showed that cluster IDPs also contain isotopically enriched ($\delta D \leqslant 25{,}000‰$; $\delta^{15}N \leqslant 480‰$) organic matter, suggesting that they too acquired interstellar organics. More recently, Busemann et al. (2006b) demonstrated that IOM separates of primitive CCs can also contain localized D and ^{15}N enrichments (up to $19{,}400 \pm 4{,}600‰$ and $1510 \pm 240‰$ in the GRO 9557 CR1 chondrite), respectively, reaching the isotopic composition of cometary ices and interstellar matter. With a maximum $\delta D = 8600 \pm 1000‰$ and $\delta^{15}N = 410 \pm 130‰$, the organic component of the Tagish Lake fragments studied here is not nearly as primitive in an isotopic sense as some of the IDPs or previously measured IOM extracted from other meteorites. Although this disparity may reflect differences in the organic reservoirs originally acquired by these objects, the minerals with which the IOM in these fragments is spatially associated strongly suggest that parent-body processing has affected its character and isotopic composition.

Virtually all of the Tagish Lake fragments that we examined contain carbonates and sheet silicates near to (tens of nm) or within the regions containing the hotspots. Although the lithology of the fragments that we report on here was originally unknown, our results indicate that these fragments experienced aqueous alteration, consistent with the previous observations (Brown et al., 2000; Zolensky et al., 2000; Keller and Flynn, 2001; Zolensky et al., 2002). Moreover, the abundant mixed-cation carbonates that occur in these fragments (e.g., Figs. 5 and 7) suggest that they were probably part of the carbonate-rich lithology, cf., Zolensky et al. (2002). If this inference is correct, then the material in these fragments experienced some of the latest stages of parent-body alteration for this lithology (Zolensky et al., 2002). Although the isotopic composition of the IOM points to an originally primitive origin, e.g., in a molecular cloud or the outer reaches of the solar protoplanetary disk where low-T reactions could have occurred (Sandford et al., 2001; Charnley and Rodgers, 2002), the IOM was certainly witness to parent-body alteration and thus susceptible to chemical modification.

We hypothesize that the relatively lower δD and ^{15}N values of the IOM in these fragments, compared to that in the meteorites and IDPs cited above, is due to isotopic exchange with the parent-body fluids which formed the spatially associated alteration phases. But which of the materials described above most likely carry the observed anomalies and what do these associations tell us about alteration processes? The region encompassing the ^{15}N hotspot in fragment 1 contains both C-rich amorphous material and serpentine (Fig. 2). The amorphous material seems to be the more likely candidate for the carrier of the ^{15}N anomaly because its short-range order and aromatic functionality (Fig. 3) are characteristics expected for a macromolecular organic carrier. However, the HRTEM images show that serpentine is abundant in the ^{15}N-rich region (Fig. 2c and d) and EDS measurements indicate C, Fe, Mg, Si, and O occur across it (Fig. 3a and b). The TEM data, therefore, suggest a mixture of a silicate and an organic component. Clay minerals are known to be capable of absorbing organic compounds (MacEwan and Wilson, 1984) and elemental mapping has revealed spatial relationships between clay-rich matrix and organic matter in several CCs, including Tagish Lake (Pearson et al., 2002). In addition, EELS measurements on clay particles in Tagish Lake show that they can contain C in a variety of functional groups, including aromatic, aliphatic, carboxylic, and carbonate forms (Garvie and Buseck, 2007). It is therefore possible that some of the ^{15}N-rich IOM in this fragment is part of a larger aromatic network that is preferentially associated with the serpentine as, perhaps, a coating

on its surface or absorbed within its structure. Further assessment of the molecular nature of the carrier of the ^{15}N anomaly is difficult. Any number of N-bearing functional groups could contain ^{15}N, and we have no direct evidence from these fragments to describe its character. We suspect that our attempts to measure N functionality were unsuccessful because the overall N abundance is low (perhaps below the detection level of our spectrometer), some N loss could have occurred during FIB-SEM preparation and STXM measurements, or some combination of these factors. We note, however, that XANES measurements on IOM residues from the GRO 95577 chondrite, which contains some of the most isotopically anomalous IOM yet studied, suggest that its ^{15}N-rich material contains abundant nitrile (C≡N) moieties (Busemann et al., 2007). Nitriles have been detected in Tagish Lake extracts (Gilmour et al., 2001) and other IOM residues (De Gregorio et al., 2010) and could be one possible carrier of the anomaly we observe.

In comparison, the region encompassing the most C-rich region in fragment 2 contains carbonate and amorphous material. The EELS and EDS measurements show that amorphous material contains abundant aromatic C (Figs. 5 and 7), consistent with an organic component. However, the EDS measurements also indicate that the amorphous region contains O, Mg, Ca, and Fe (Figs. 5 and 7), suggesting a mixture of an organic and a carbonate-like component. The presence of metal cations within the amorphous material is somewhat unexpected for an organic component. Three possible explanations are: (1) the amorphous material is actually carbonate that was amorphized under the SIMS or FIB ion beams; (2) the re-deposition of material during ion milling; or (3) fine-scale intergrowth of organics and carbonate through the thickness of the section that are not fully resolved in the images. We rule out ion-beam amorphization because the HAADF and HRTEM images indicate that in some places the amorphous material of similar composition extends >200 nm below the Pt strap, which is well beyond the tens-of-nanometers range of 30 kV Ga^+ and 15 kV ion-beam damage, and even fills in space between crystalline grains where it was exposed to the ion beam. Furthermore, crystalline material remains intact in some areas where the Pt was completely eroded (Fig. 6, white arrowhead). Although some re-deposition of sputtered material does occur on the surface, as demonstrated by the appearance of Au in the spectra of the carbonate and amorphous material, this re-deposited layer comprises <10% of the sample thickness. In order to match the C:Mg ratio of the amorphous material (Fig. 5b–1 and 2) with a mixture of pure C and carbonate (Fig. 5b–5), a ratio of approximately two parts C to one part carbonate is required, i.e., re-deposited carbonate would comprise 1/3 of the section volume. A fine-scale intergrowth of organics and a carbonate component, as suggested by the irregular grain boundaries in the HAADF image (Fig. 5a), is more likely. These data, therefore, suggest a possible spatial and genetic relationship between the carbonates and the enriched IOM. If these mixed-cation carbonates were indeed formed through *in situ* aqueous alteration in the parent body, as comparison with previous studies suggest (Nakamura et al., 2003; Zolensky et al., 2002), then the IOM could have been a possible C source for carbonate formation. Cody and Alexander (2005) provide one possible pathway for carbonate formation from IOM. Briefly, a methylene group in the IOM could have become progressively oxidized by hydroxy radicals to alcohol, ketone, carboxyl, and ultimately, bicarbonate groups (see Fig. 8 of Cody and Alexander, 2005). The bicarbonate could then have reacted with cations in the aqueous fluid to form the carbonates in these matrix fragments. Previous analyses of the soluble organic fraction from the Tagish Lake CC have suggested that a relationship between organics and abundant carbonates might exist (Pizzarello et al., 2006). The spatial association of crystalline carbonate, C-rich IOM, and an amorphous carbonate-like component in these Tagish Lake fragments is consistent with such a relationship and suggests a partially arrested alteration reaction. However, given the high solubility of bicarbonate, it is unclear why carbonate grains would necessarily form in spatial association with the IOM rather than be transported elsewhere in the matrix. A possible explanation is a local change in fluid chemistry whereby the pH was sufficiently high to precipitate carbonate from the solution. Similar arguments were invoked to explain the occurrence of carbonates outside of chondrules in the matrix of CM chondrites, i.e., Ca leached from the glass encountered more alkaline fluid on the chondrule exterior whereby carbonate precipitation occurred (Brearley, 2006).

Owing to the mobility of H and the difficulty in detecting it, assigning a molecular carrier for the H anomalies we observe is simply not possible at this time. D is very likely part of the amorphous aromatic network composing the IOM in these fragments, e.g., the solid amorphous material on the right side of fragment 2 (Fig. 8b), but the XANES measurements do not permit molecular speciation. Some inorganic phases may also be carriers of the D anomalies. For example, a D hotspot correlates with what appear to be sheet silicates in at least one of the samples, e.g., the right-most side of fragment 3 (Fig. 9b and d). Whether D-rich sheet silicates could have formed in interstellar clouds is not known, but we suspect that this too is more likely a parent-body signature. It is conceivable that some D, perhaps initially part of discrete IOM grains (e.g., nanoglobules) that accreted with other matrix materials in the Tagish Lake CC, could have been redistributed during parent-body alteration and incorporated into the hydroxyl groups of the serpentine structure. Such isotopic exchange between organics and the altering fluid(s) to produce sheet silicates was considered to explain heterogeneities in the D/H ratios measured from matrix and fine-grained rim materials of CR chondrites (Bonal et al., 2010), but without complete mineralogic characterization of the isotopic hotspots. Future *in situ* studies of isotopically anomalous IOM might reveal whether or not there is a trend of D hotspots correlating with sheet silicates, i.e., D-rich sheet silicates spatially associated with D-rich IOM. Nonetheless, the spatially associated alteration phases and isotopically anomalous organics cited here lends credence to the idea that chondrites could have acquired a common IOM precursor whose compositional variations among the various classes

are due to asteroidal processing (Alexander et al., 2007, 2010).

5. CONCLUSIONS

SIMS analysis of fragments of the Tagish Lake carbonaceous chondrite has revealed areas ranging from hundreds to thousands of nanometers in size that are enriched in isotopes of H and N (isotopic hotspots) relative to terrestrial standards. The spatial correlation of several of the isotopic hotspots with elevated C abundance suggests that they are contained within an organic component. A precursor of this organic component, common to all chondrites (Alexander et al. 2007), may have originated in interstellar clouds or in the outer reaches of the solar protoplanetary disk where low-T reactions capable of extreme isotopic enrichment were possible. TEM analyses, enabled by site-specific FIB extraction of the H and N hotspots in four fragments from the Tagish Lake chondrite, reveal that they contain an amorphous component, sheet silicates, carbonates, and sulfides. EDS shows that the amorphous component contains abundant C, and EELS and XANES show that it contains abundant aromaticity. We suspect that this component is macromolecular in nature, is likely the major carrier material of the isotopic anomalies we observe, and is probably the same material that has been extracted in residue form from bulk samples as insoluble organic matter (IOM) (Busemann et al., 2006b; Alexander et al., 2007). The spatial association of the organic material with phases formed through low-temperature aqueous-alteration on the Tagish Lake parent body suggests that it was probably susceptible to the effects of alteration, i.e., isotopic exchange between the organics and altering fluid. The large spatial extent of some of the D enrichments suggests the possibility that hydroxyl in sheet silicates may be carriers of the D, but we cannot rule out that the anomalous H could be part of an organic material intergrown with the sheet silicates. The juxtaposition of carbonates and organic material in at least one of the fragments lends credence to the idea that the latter might have provided a source of C for the former, but such a spatial association would likely require locally higher pH in order for carbonate to precipitate, e.g., a microchemical environment (Brearley, 2006). Nonetheless, that isotopic anomalies are preserved in the IOM indicates that the organics must have been sufficiently robust to isotopic equilibration.

ACKNOWLEDGMENTS

We thank Mike Zolensky for the samples of the Tagish Lake CC and Laurence Garvie for the reference samples of calcite, diamond, and graphite. We also thank them, Adrian Brearley, two anonymous referees, and AE Sandra Pizzarello for suggestions that improved the manuscript. We appreciate the assistance of Sue Wirick in setting up XANES experiments and Brad De Gregorio in processing XANES data. This research was supported by grants from the NASA Astrobiology, Cosmochemistry, and Origins of Solar Systems programs. A. Young was supported by a NSF Research Experience for Undergraduates Program at the Carnegie Institution.

REFERENCES

Alexander C. M. O'D., Russell S. S., Arden J. W., Ash R. D., Grady M. M. and Pillinger C. T. (1998) The origin of chondritic macromolecular organic matter: a carbon and nitrogen isotope study. *Meteor. Planet. Sci.* **33**, 603–622.

Alexander C. M. O'D., Fogel M., Yabuta H. and Cody G. D. (2007) The origin and evolution of chondrites recorded in the elemental and isotopic compositions of their macromolecular organic matter. *Geochim. Cosmochim. Acta* **71**, 4380–4403.

Alexander C. M. O'D., Newsome S. N., Fogel M. L., Nittler L. R., Busemann H. and Cody G. D. (2010) Deuterium enrichments in chondritic macromolecular material – implications for the origin and evolution of organics, water and asteroids. *Geochim. Cosmochim. Acta* **74**, 4417–4437.

Ashley J. W., Huss G. R., Garvie L. A. J., Guan Y., Buseck P. R. and Williams L. B. (2005) Nitrogen and carbon isotopic measurements of carbonaceous nanoglobules from the Tagish Lake meteorite by secondary ion mass spectrometry. *Lunar Planet. Sci. XXXVI*. Lunar Planet. Inst., Houston #2205 (abstr.).

Bassim N. D., De Gregorio B. T., Kilcoyne A. L. D., Scott K., Chou T., Wirick S., Cody G. D., Fischione P., Liu J. and Stroud R. M. (2010) Towards low-damage TEM sample preparation of carbonaceous materials in the focused ion beam. *Microsc. Microanal.* **15**(Suppl. 2), 342–343.

Bonal L., Huss G. R. and Nagashima K. (2010) Hydrogen isotopic composition of the water in CR chondrites. *Lunar and Planetary Science XLI*. Lunar Planet. Inst., Houston #1442 (abstr.).

Brearley A. J. (2005) Nebular versus parent-body processing. In *Meteorites, Comets, and Planets* (ed. A. M. Davis) vol. 1 *Treatise on Geochemistry* (eds. H. D. Holland and K. K. Turekian), Elsevier-Pergamon, Oxford, pp. 247–268.

Brearley A. J. (2006) The role of microchemical environments in the alteration of CM carbonaceous chondrites. *Lunar Planet. Sci. XXXVII*. Lunar Planet. Inst., Houston #2074 (abstr.).

Brown P. G., Hildebrand A. R., Zolensky M. E., Grady M., Clayton R. N., Mayeda T. K., Tagliaferri W., Spalding R., MacRae N. D., Hoffman E. L., Mittlefehldt D. W., Wacker J. F., Bird J. A., Campbell M. D., Carpenter R., Gingerich H., Glatiotis M., Greiner E., Mazur M. J., McCausland P. J., Plotkin H. and Mazur T. R. (2000) The fall, recovery, orbit, and composition of the Tagish Lake Meteorite: a new type of carbonaceous chondrite. *Science* **290**, 320–325.

Busemann H., Alexander C. M. O'D., Nittler L. R., Zega T. J., Stroud R. M., Cody G. D. and Yabuta H. (2006a) Correlated microscale isotope and scanning transmission X-ray analyses of isotopically anomalous organic matter from the CR2 chondrite EET 92042. *Lunar Planet. Sci. XXXVII*. Lunar Planet. Inst., Houston #2005 (abstr.).

Busemann H., Young A. F., Alexander C. M. O'D., Hoppe P., Mukhopadhyay S. and Nittler L. R. (2006b) Interstellar chemistry recorded in organic matter from primitive meteorites. *Science* **312**, 727–730.

Busemann H., Zega T. J., Alexander C. M. O'D., Cody G. D., Kilcoyne A. L. D., Nittler L. R., Stroud R. M. and Yabuta H. (2007) Secondary ion mass spectrometry and X-ray absorption near-edge structure spectroscopy of isotopically anomalous organic matter from CR1 chondrite GRO 95577. *Lunar Planet. Sci. XXXVIII*. Lunar Planet. Inst., Houston #1884 (abstr.).

Charnley S. B. and Rodgers S. D. (2002) The end of interstellar chemistry as the origin of nitrogen in comets and meteorites. *Astrophys. J.* **569**, L133–L137.

Cody G. D., Ade H., Alexander C. M. O'D., Araki T., Butterworth A., Fleckenstein H., Flynn G. J., Gilles M. K., Jacobsen C., Kilcoyne A. L. D., Messenger K., Sandford S. A., Tyliszczak T., Westphal A. J., Wirick S. and Yabuta H. (2008) Quantitative organic and light-element analysis of comet 81P/Wild 2 particles using C-, N-, and O-m-XANES. *Meteorit. Planet. Sci.* **43**, 353–365.

Cody G. D. and Alexander C. M. O'D. (2005) NMR studies of chemical structural variation of insoluble organic matter from different carbonaceous chondrite groups. *Geochim. Cosmochim. Acta* **69**, 1085–1097.

Connolly, Jr., H. C., Desch S. J., Ash R. D. and Jones R. H. (2006) Transient heating events in the protoplanetary nebula. In *Meteorites and The Solar System II* (eds. D. S. Lauretta and H. Y. McSween Jr.). The University of Arizona Press, Tucson, AZ, pp. 383–397.

De Gregorio B. T., Stroud R. M., Nittler L. R., Alexander C. M. O'D., Kilcoyne A. L. D. and Zega T. J. (2010) Isotopically anomalous organic nanoglobules from Comet81P/Wild 2. *Geochim. Cosmochim. Acta* **74**, 4454–4470.

Egerton R. F. (1996) *Electron Energy-loss Spectroscopy in The Electron Microscope*. Plenum Press, New York, pp. 485.

Floss C. and Stadermann F. J. (2009) High abundances of circumstellar and interstellar C-anomalous phases in the primitive CR3 chondrite QUE 99177 and MET 00426. *Astrophys. J.* **697**, 1242–1255.

Garvie L. A. J., Baumgardner G. and Buseck P. R. (2008) Scanning electron microscopical and cross-sectional analysis of extraterrestrial carbonaceous nanoglobules. *Meteorit. Planet. Sci.* **43**, 899–903.

Garvie L. A. J. and Buseck P. R. (2004) Nanosized carbon-rich grains in carbonaceous chondrite meteorites. *Earth Planet. Sci. Lett.* **224**, 431–439.

Garvie L. A. J. and Buseck P. R. (2007) Prebiotic carbon in clays from Orgueil and Ivuna (CI) and Tagish Lake (C2 ungrouped) meteorites. *Meteorit. Planet. Sci.* **42**, 2111–2117.

Gilmour I. (2005) Structural and isotopic analysis of organic matter in carbonaceous chondrites. In *Meteorites, comets, and planets* (ed. A. M. Davis) vol. 1 *Treatise on Geochemistry* (eds. H. D. Holland and K. K. Turekian), Elsevier, New York, pp. 269–290.

Gilmour I., Sephton M. A. and Pearson V. K. (2001) The Tagish Lake chondrite and the interstellar parent body hypothesis. *Lunar Planet. Sci. XXXII*. Lunar Planet. Inst., Houston #1969 (abstr.).

Grady M. M., Verchovsky A. B., Franchi I. A., Wright I. P. and Pillinger C. T. (2002) Light element geochemistry of the Tagish Lake CI2 chondrite: comparison with CI1 and CM2 meteorites. *Meteorit. Planet. Sci.* **37**, 713–735.

Herd C. D. K., Nittler L. R. and Alexander C. M. O'D. (2009) Isotopically heterogeneous organic matter in the Tagish Lake meteorite. *Lunar Planet. Sci. XL*. Lunar Planet. Inst., Houston #1818 (abstr.).

Hitchcock A. P. and Mancini D. C. (1994) Bibliography and databases of inner shell excitation spectra of gas phase atoms and molecules. *J. Electron. Spectrosc.* **67**, 1–123.

Hovmöller S. (1992) Crisp – crystallographic image-processing on a personal-computer. *Ultramicroscopy* **41**, 121–135.

Keller L. P. and Flynn G. J. (2001) Matrix mineralogy of the Tagish Lake carbonaceous chondrite: TEM and FTIR studies. *Lunar Planet. Sci. XXXII*. Lunar Planet. Inst., Houston #1639 (abstr.).

MacEwan D. M. C. and Wilson M. J. (1984) Interlayer and intercalation complexes of clay minerals. In *Crystal Structures of Clay Minerals and their X-ray Identification. Monograph 5* (eds. G. Brown and G. W. Brindley). Mineralogical Society, London, pp. 197–248.

MacPherson G. J. (2005) Calcium–Aluminum-rich inclusions in chondritic meteorites. In *Meteorites, Comets, and Planets* (ed. A. M. Davis) vol. 1 *Treatise on Geochemistry* (eds. H. D. Holland and K. K. Turekian), Elsevier, New York. pp. 201–246.

Messenger S. (2000) Identification of molecular-cloud material in interplanetary dust particles. *Nature* **404**, 968–971.

Messenger S., Nakamura K., Nittler L. R. and Young A. F. (2004) Nitrogen isotopic imaging of Tagish Lake carbon globules. *Lunar Planet. Sci. XXXV*. Lunar Planet. Inst., Houston #1347 (abstr.).

Nakamura-Messenger K., Messenger S., Keller L. P., Clemett S. J. and Zolensky M. E. (2006) Organic globules in the Tagish Lake meteorite: Remnants of the protosolar disk. *Science* **314**, 1439–1442.

Nakamura K., Messenger S., Keller L. P., Flynn G. J., and Wirick S. (2004) Organic globules with anomalous nitrogen isotopic compositions in the Tagish Lake meteorite: products of primitive organic reactions. *Workshop on Chondrites and Protoplanetary Disk*, Lunar and Planet. Inst., Houston #9067 (abstr.).

Nakamura K., Zolensky M. E., Tomita S., Nakashima S. and Tomeoka K. (2002) Hollow organic globules in the Tagish Lake meteorite as possible products of primitive organic reactions. *Int. J. Astrobiol.* **1**, 179–189.

Nakamura T., Noguchi T., Zolensky M. E. and Tanaka M. (2003) Mineralogy and noble-gas signatures of the carbonate-rich lithology of the Tagish Lake carbonaceous chondrite. *Earth Planet. Sci. Lett.* **207**, 83–101.

Pearson V. K., Sephton M. A., Kearsley A., Bland P. A., Franchi I. A. and Gilmour I. (2002) Clay mineral-organic matter relationships in the early solar system. *Meteorit. Planet. Sci.* **37**, 1829–1833.

Pizzarello S., Cooper G. W. and Flynn G. J. (2006) The nature and distribution of the organic material in carbonaceous chondrites and interplanetary dust particles. In *Meteorites and the Early Solar System II* (eds. D. S. Lauretta and H. Y. McSween Jr.). The University of Arizona Press, Tucson, pp. 625–651.

Pizzarello S., Huang Y., Becker L., Poreda R. J., Nieman R. A., Cooper G. W. and Williams M. (2001) The organic content of the Tagish Lake meteorite. *Science* **293**, 2236–2239.

Remusat L., Robert F., Meibom A., Mostefaoui S., Delpoux O., Binet L., Gourier D. and Derenne S. (2009) Proto-planetary disk chemistry recorded by D-rich organic radicals in carbonaceous chondrites. *Astrophys. J.* **698**, 2087–2092.

Robert F. and Epstein S. (1982) The concentration and isotopic composition of hydrogen, carbon, and nitrogen in carbonaceous chondrites. *Geochim. Cosmochim. Acta* **46**, 81–95.

Sandford S. A., Bernstein M. P. and Dworkin J. P. (2001) Assessment of the interstellar processes leading to deuterium enrichment in meteoritic organics. *Meteorit. Planet. Sci.* **36**, 1117–1133.

Stadelmann P. A. (1987) Ems – a software package for electron-diffraction analysis and HREM image simulation in materials science. *Ultramicroscopy* **21**, 131–145.

Yang J. and Epstein S. (1983) Interstellar organic matter in meteorites. *Geochim. Cosmochim. Acta* **47**, 2199–2216.

Zega T. J., Nittler L. R., Busemann H., Hoppe P. and Stroud R. M. (2007) Coordinated isotopic and mineralogic analyses of planetary materials enabled by in situ lift-out with a focused ion beam scanning electron microscope. *Meteorit. Planet. Sci.* **42**, 1373–1386.

Zinner E. K. (2005) Presolar grains. In *Meteorites, comets, and planets* (ed. A. M. Davis) vol. 1 *Treatise on Geochemistry* (eds. H. D. Holland and K. K. Turekian), Elsevier, New York, pp. 17–39.

Zolensky M. E., Grady M. M., Clayton R. N., Mayeda T. K., Hildebrand A. R., Brown P. G., Brook J. L. and Roots C. F. (2000) Tagish Lake: a special new type 2 carbonaceous chondrite fall. *Meteorit. Planet. Sci.* **35**, A178–179.

Zolensky M. E., Nakamura K., Gounelle M., Mikouchi T., Kasama T., Tachikawa O. and Tonui E. (2002) Mineralogy of Tagish Lake: an ungrouped type 2 carbonaceous chondrite. *Meteorit. Planet. Sci.* **37**, 737–761.

Associate editor: Sandra Pizzarello